AIMS Mathematics, 11(6): 17208–17238.
DOI:10.3934/math.2026706
Received: 18 March 2026
Revised: 19 May 2026
Accepted: 29 May 2026
Published: 15 June 2026

https://www.aimspress.com/journal/Math

Research article

Variational mode decomposition optimized by the tornado optimization algorithm combined with wavelet thresholding for neuronal spike signal denoising

Can Ma[1,2], **Zuozhi Liu**[1,2,3,*] **and Hui Li**[1,2]

[1] School of Mathematics and Statistics, Guizhou University of Finance and Economics, Guiyang 550025, China

[2] School of Big Data Statistics, Guizhou University of Finance and Economics, Guiyang 550025, China

[3] School of Mathematics, Northwest University, Xi'an 710069, China

* **Correspondence:** Email: liuzuo.zhi@163.com.

Abstract: Neuronal spikes are carriers of neural information, and high-quality recordings are critical for neural coding and brain-computer interface research. However, electrophysiological recordings are often corrupted by noise, reducing the signal-to-noise ratio (SNR) and distorting spike waveforms. Although variational mode decomposition (VMD) is suitable for non stationary neural signal processing, its performance relies heavily on manual selection of mode number K and penalty factor α, resulting in poor adaptability. This paper proposes a neuronal spike denoising method combining tornado optimizer with Coriolis force (TOC)-optimized VMD and wavelet thresholding. With Hilbert envelope entropy as the fitness function, TOC adaptively optimizes VMD parameters; the kurtosis criterion separates signal-dominant and noise-dominant components; wavelet thresholding further denoises noise-dominant parts to reconstruct purified spike signals from valid components. Experiments on simulated and real neuronal signals verify that the proposed method outperforms classic empirical mode decomposition, conventional VMD and particle swarm optimization-VMD. Specifically, on real signals, it improves the SNR by 14.0322 dB, reduces mean absolute error by 0.0815 and root mean square error by 0.1102, raises the normalized cross-correlation by 0.0494 and the energy SNR by 6.30%. The proposed method effectively suppresses noise while preserving spike waveform features, providing high-quality data for subsequent spike sorting and neural decoding.

Keywords: variational mode decomposition; tornado optimizer with Coriolis force; wavelet thresholding; Hilbert envelope entropy; kurtosis; neuronal spike signal denoising
Mathematics Subject Classification: 65T60, 92C20, 94A12

1. Introduction

Neuronal spikes are transient electrical signals generated by neuronal action potentials, which provide critical information for neural coding, circuit function analysis, and brain-computer interface development [1, 2]. High-quality raw signals are the fundamental prerequisite for accurately detecting spike firing times, extracting waveform features, and interpreting neural information. However, in practical electrophysiological recordings, spike signals are often corrupted by various noise sources, such as instrumental noise, background neural activity, and power line interference [3, 4]. Such noise reduces the signal-to-noise ratio (SNR), distorts waveforms, causes misdetection of spikes, and decreases the accuracy of signal sorting and decoding [5, 6]. Therefore, developing effective denoising methods is regarded as an important fundamental task in neural signal processing.

Existing denoising methods for neuronal spikes mainly include frequency-domain filtering, time-domain averaging, and wavelet threshold denoising [7]. Frequency-domain filtering is simple to implement, but its denoising performance deteriorates significantly when the noise spectrum overlaps with the spike frequency band [8]. Time-domain averaging requires repeated waveform alignment and performs poorly on non stationary signals or those with a low firing rate [9]. Wavelet threshold denoising can handle non-stationary signals, but its performance greatly depends on the selection of the wavelet basis, decomposition level, and threshold strategy, resulting in limited adaptability [10, 11]. In recent years, adaptive signal decomposition methods have provided new solutions for denoising non-stationary signals [12, 13]. Among these, empirical mode decomposition (EMD) suffers from mode mixing and end effects, which affect the stability of the decomposition results [14, 15]. Variational mode decomposition (VMD) can achieve stable band-constrained decomposition and effectively alleviate mode mixing; thus, it is more suitable for processing non stationary signals such as neuronal spikes. Nevertheless, the performance of VMD strongly depends on the settings of the mode number K and the penalty factor α. Improper parameter settings lead to over- or under decomposition [16, 17], while traditional parameter selection methods mostly rely on manual experience or a grid search, with the drawbacks of poor adaptability and high computational cost.

To address the above problems, many studies have combined VMD with wavelet threshold denoising to construct a joint denoising framework [18–21]. Such methods have improved denoising performance compared with single approaches, but they still have obvious limitations. On the one hand, the key parameters of VMD are usually set empirically and cannot be adaptively adjusted with noise levels. On the other hand, fixed wavelet thresholds struggle to balance noise suppression and signal detail preservation, easily leading to incomplete denoising or waveform distortion.

Intelligent optimization algorithms provide a feasible way to adaptively optimize VMD parameters [22]. Classical algorithms such as particle swarm optimization (PSO) and the grey wolf optimizer (GWO) have been applied to reduce the subjectivity of manual parameter tuning [23, 24]. However, PSO is prone to premature convergence [25], the GWO lacks precision in high-dimensional optimization scenarios [26], and multi objective optimization methods suffer from complex parameter settings and high computational costs [27]. These issues make it difficult for them to meet the dual requirements of accuracy and efficiency in neuronal spike denoising. Meanwhile, the issues of uncertainty and insufficient robustness during parametric optimization have also been widely recognized in complex decision-making tasks [28, 29], further limiting the performance of traditional optimization methods in practical neural spike denoising.

The tornado optimizer with Coriolis force (TOC) is a novel metaheuristic inspired by tornadoes' dynamics, involving the Coriolis effect and rotating airflow [30]. With fast convergence, strong global search ability, and simple parameter settings, TOC offers favorable adaptability to complex nonlinear optimization problems [31], providing a new approach to adaptive parameter optimization in VMD.

Based on the abovementioned research background, our main motivation in this paper is to investigate effective denoising approaches for non stationary neuronal spike signals, focusing on addressing the issues of manual parameter tuning, poor adaptability to decomposition, and incomplete noise suppression in traditional denoising methods. The main contributions of this paper include the following three aspects.

(1) A novel denoising framework combining TOC-optimized VMD with wavelet soft thresholding is proposed for neuronal spike signals, integrating adaptive parameter optimization, modal component classification, and secondary noise reduction to achieve a better balance between noise suppression and waveform preservation.
(2) The TOC algorithm is utilized to adaptively optimize the mode number K and penalty factor α of VMD with Hilbert envelope entropy as the fitness function, which effectively reduces the subjectivity and uncertainty caused by traditional manual parameter selection and improves the decomposition stability.
(3) A two-stage denoising mechanism using the kurtosis criterion and wavelet soft threshold is designed to separate the signal and noise components and further purify the noise components while retaining detailed morphological features of the spikes. Comprehensive experiments using statistical significance tests are conducted on simulated signals with varying noise levels and on real electrophysiological recordings. The results confirm that the proposed method significantly outperforms several classical denoising methods in multiple evaluation metrics and maintains satisfactory computational efficiency.

The remainder of this paper is organized as follows. Section 2 introduces the basic principles of VMD, the TOC algorithm, envelope entropy, and wavelet threshold denoising. Section 3 describes the workflow of the proposed denoising framework in detail. Section 4 evaluates the method's performance using both simulated and real neuronal recording signals and compares it with several related denoising methods. Finally, Section 5 summarizes the work and presents potential directions for future research.

2. Preliminaries

2.1. Variational mode decomposition

VMD is a self-adaptive technique for decomposing non-stationary electrophysiological signals in the frequency domain. Its core idea is to split the noisy spike signal $f(t)$ into K band-limited intrinsic mode functions (IMFs). These IMFs have slowly varying amplitudes and phases. We build a constrained variational model to achieve this decomposition. This method matches the narrow-band spectral features of spikes, and its basic form is

$$u_k(t) = A_k(t)\cos(\varphi_k(t))\,. \tag{2.1}$$

Here, $A_k(t)$ is the instantaneous amplitude of the k-th IMF, and $\varphi_k(t)$ is the instantaneous phase. Both of them change slowly over time. We get the instantaneous frequency by calculating the derivative of

the phase with respect to time

$$\omega_k(t) = \frac{\mathrm{d}\varphi_k(t)}{\mathrm{d}t}. \tag{2.2}$$

The primary optimization objective of VMD is to minimize the overall bandwidth of all IMFs. Meanwhile, we must ensure that the superposition of all components can recover the original signal. Mathematically, we use the Hilbert transform to perform an analytic extension on $u_k(t)$, yielding a one-sided spectrum that exclusively contains positive frequencies

$$\left(\delta(t) + \frac{j}{\pi t}\right) * u_k(t). \tag{2.3}$$

Then the spectrum of the resulting analytic signal is shifted to the baseband associated with the central frequency ω_k via the complex exponential term $e^{-j\omega_k t}$, thereby enabling spectral segregation of distinct constituent parts

$$\left[\left(\delta(t) + \frac{j}{\pi t}\right) * u_k(t)\right] e^{-j\omega_k t}. \tag{2.4}$$

Finally, we use the L_2-norm of the first-order temporal derivative to quantify the bandwidth of each mode, and formulate the constrained variational framework presented below

$$\begin{cases} \min_{\{u_k\},\{\omega_k\}} \left\{ \sum_{k=1}^{K} \left\| \partial_t \left[\left(\delta(t) + \frac{j}{\pi t}\right) * u_k(t) \right] e^{-j\omega_k t} \right\|_2^2 \right\}, \\ \text{s.t.} \quad \sum_{k=1}^{K} u_k(t) = f(t), \end{cases} \tag{2.5}$$

where $\{u_k\} = \{u_1, u_2, \ldots, u_K\}$ denote the modal constituents yielded by the decomposition process, $\{\omega_k\} = \{\omega_1, \omega_2, \ldots, \omega_K\}$ represent their corresponding central frequencies, $\delta(t)$ signifies the Dirac delta function, j stands for the imaginary unit, and "*" denotes the convolution operator.

To solve this constrained variational formulation, we introduce the quadratic penalty coefficient α and Lagrange multiplier function $\lambda(t)$ to construct the augmented Lagrangian functional $\mathcal{L}$. This transforms the original constrained optimization task into an unconstrained variational optimization framework

$$\begin{aligned} \mathcal{L}(\{u_k\}, \{\omega_k\}, \lambda) = \alpha \sum_{k=1}^{K} \left\| \partial_t \left[\left(\delta(t) + \frac{j}{\pi t}\right) * u_k(t) \right] e^{-j\omega_k t} \right\|_2^2 \\ + \left\| f(t) - \sum_{k=1}^{K} u_k(t) \right\|_2^2 + \left\langle \lambda(t), f(t) - \sum_{k=1}^{K} u_k(t) \right\rangle. \end{aligned} \tag{2.6}$$

Here, α balances the bandwidth estimation fidelity and signal reconstruction accuracy, and controls the strength of the bandwidth constraint. The Lagrange multiplier $\lambda(t)$ ensures that the reconstruction constraint is strictly satisfied mathematically.

VMD uses the alternate direction method of multipliers (ADMM) to iteratively find the saddle point of the augmented Lagrangian function. It updates the mode component u_k and center frequency ω_k in the frequency domain. The update formulas are

$$\hat{u}_k^{n+1} = \frac{\hat{f}(\omega) - \sum_{i=1,i<k}^{K} \hat{u}_i^{n+1}(\omega) - \sum_{i=1,i>k}^{K} \hat{u}_i^{n}(\omega) + \frac{\hat{\lambda}(\omega)}{2}}{1 + 2\alpha(\omega - \omega_k^n)^2}. \tag{2.7}$$

$$\hat{\omega}_k^{n+1} = \frac{\int_0^\infty \omega |\hat{u}_k^{n+1}(\omega)| d\omega}{\int_0^\infty |\hat{u}_k^{n+1}(\omega)| d\omega}. \tag{2.8}$$

The iterative update law for the Lagrange multiplier function is given by

$$\hat{\lambda}^{n+1}(\omega) = \hat{\lambda}^n(\omega) + \tau \left[\hat{f}(\omega) - \sum_{k=1}^{K} \hat{u}_k^{n+1}(\omega) \right], \tag{2.9}$$

where $\hat{u}_k$, $\hat{f}$, and $\hat{\lambda}$ denote the Fourier transforms of u_k, f, and $\lambda(t)$, respectively; n denotes the iteration index; and $\tau > 0$ represents the learning rate. The iterative procedure proceeds until the convergence criterion is satisfied

$$\sum_{k=1}^{K} \frac{\left\| \hat{u}_k^{n+1} - \hat{u}_k^n \right\|_2^2}{\left\| \hat{u}_k^n \right\|_2^2} < \varepsilon. \tag{2.10}$$

Here, ε is the convergence precision, and it is usually set to $10^{-6} \sim 10^{-7}$ in practical implementations.

2.2. Tornado optimizer with Coriolis force

TOC is a population-based global optimization algorithm. It draws inspiration from the Coriolis effect and the rotation of airflow in tornadoes. It strikes an excellent balance between global exploration and local exploitation, making it well-suited for intricate nonlinear multi parameter optimization tasks.

In the TOC algorithm, each potential solution is conceptualized as a "storm", and the entire collection of storms comprises the search population. We divide storms into tornadoes, thunderstorms, and ordinary storms according to their fitness values. This guides the population to evolve toward the global optimum.

First, initialize a population of n_w storms, each representing a d-dimensional candidate solution. The population is expressed as a $n_w \times d$ matrix y_w

$$y_w = \begin{bmatrix} y_{w_1} & y_{w_2} & \cdots & y_{w_i} & \cdots & y_{w_{n_w}} \end{bmatrix} = \begin{bmatrix} y_{w_{1,1}} & y_{w_{1,2}} & \cdots & y_{w_{1,d}} \\ y_{w_{2,1}} & y_{w_{2,2}} & \cdots & y_{w_{2,d}} \\ \vdots & \vdots & \vdots & \vdots \\ y_{w_{n_w,1}} & y_{w_{n_w,2}} & \cdots & y_{w_{n_w,d}} \end{bmatrix} \tag{2.11}$$

For VMD parameter optimization, the 2-dimensional position vector of each storm maps directly to the VMD parameter pair (K, α).

During iteration, we calculate each storm's fitness and rank storms into tornadoes, thunderstorms, and ordinary storms. We design a fitness-based storm allocation mechanism to improve efficiency. The number of storms assigned to the k-th thunderstorm/tornado n_{w_k} is

$$n_{w_k} = \left| \left(\frac{fit_k - fit_o + 1}{\sum_{k=1}^{n_{w_0}} (fit_k - fit_o + 1)} \right) \times n_w \right|. \tag{2.12}$$

Here, fit_k denotes the fitness of the k-th thunderstorm, while fit_o represents the fitness value of the dominant tornado. This mechanism provides more search agents to find better solutions, thereby improving global search efficiency.

Based on the three-force balance of Coriolis force, the centrifugal force, and the pressure gradient force in atmospheric turbulence, a storm velocity update model is constructed

$$\vec{v}_i^{t+1} = \eta\left(\mu\vec{v}_i^{t} - c\frac{f \times R}{2} + \sqrt{CF}\right). \tag{2.13}$$

Here, $\vec{v}_i^{t+1}$ represents the iteratively updated velocity of the i-th storm, while $\vec{v}_i^{t}$ denotes its velocity at the present iteration step; μ is the inertia coefficient; c is the random coefficient; f, R, and CF are parameters that simulate the Coriolis and curvature effects; and η is the shrinkage factor, which we use to control the convergence speed of the algorithm.

Different position update strategies are designed for global exploration and local exploitation

- Learning from the tornado:

$$\vec{y}_{w_i}^{t+1} = \vec{y}_{w_i}^{t} + 2\beta\left(\vec{y}_o^{t} - rand_w\right) + \vec{v}_i^{t+1}, \tag{2.14}$$

  where $\vec{y}_o^{t}$ is the tornado's position vector, and $rand_w$ is a random number in [0, 1], enabling a deep local search around the optimal solution.
- Learning from thunderstorms:

$$\vec{y}_{w_j}^{t+1} = \vec{y}_{w_j}^{t} + 2r_1\left(\vec{y}_{t_j}^{t} - \vec{y}_{w_j}^{t}\right) + 2r_2\left(\vec{y}_o^{t} - \vec{y}_{w_j}^{t}\right), \tag{2.15}$$

  where $\vec{y}_{t_j}^{t}$ is the thunderstorm's position vector, and r_1, r_2 are random numbers in [0, 1], enabling the global search to escape the local optima.

For the VMD parameter-tuning task, we adopt the aggregate envelope entropy as the core objective function within the TOC framework. Through an iterative search, we minimize this function to get the best VMD parameter combination (K^*, α^*). This provides good parameter support for VMD.

2.3. Hilbert envelope entropy

Hilbert envelope entropy is an information-theoretic index that we use to measure the complexity of a signal. It measures the randomness and regularity of a signal by calculating the information entropy of its envelope's amplitude distribution, thus distinguishing deterministic signals from random noise. Deterministic signals have concentrated envelope amplitudes and low envelope entropy, while random noise has uniformly distributed envelope amplitudes and high envelope entropy, thus making it an ideal objective function for VMD parameter optimization.

For a single IMF component $x(t)$ after VMD decomposition, the main steps used to compute envelope entropy are

First, we apply the Hilbert transform to the signal to get its analytic form. The Hilbert transform is defined as

$$\hat{x}(t) = \mathcal{H}[x(t)] = \frac{1}{\pi}\text{P.V.}\int_{-\infty}^{\infty}\frac{x(\tau)}{t-\tau}d\tau = x(t) * \frac{1}{\pi t}, \tag{2.16}$$

where P.V. stands for the Cauchy principal value integral, τ is the integration variable, and "*" means convolution.

We get the analytic signal $z(t)$ after applying the Hilbert transform, which is

$$z(t) = x(t) + j\hat{x}(t) = A(t)e^{j\phi(t)}. \tag{2.17}$$

Here, $\phi(t)$ is the instantaneous phase, and $A(t)$ is the envelope sequence.

Next, we normalize the envelope sequence $A(t)$ to get the probability distribution of envelope amplitudes

$$p_i = \frac{A(t_i)}{\sum_{j=1}^{N} A(t_j)}. \tag{2.18}$$

Here, N denotes the total number of sampling points of the signal, and the probabilities adhere to $\sum_{i=1}^{N} p_i = 1$.

On the basis of this distribution, we calculate the envelope entropy as follows

$$E = -\sum_{i=1}^{N} p_i \log_2 p_i. \tag{2.19}$$

For VMD parameter optimization, the sum of the envelope entropies of K BLIMF components is used as the objective function of TOC

$$F(K, \alpha) = \sum_{k=1}^{K} E_k. \tag{2.20}$$

The optimization goal of TOC is to identify the optimal parameter pair (K^*, α^*) that makes $F(K, \alpha)$ as small as possible. This way, we concentrate the signal energy into low-entropy components and spread the noise energy into high-entropy components. This helps us separate the signal and noise well in the frequency domain.

2.4. Wavelet threshold denoising

For noise-dominant IMF components $u_n(t)$ after VMD decomposition, the wavelet soft thresholding method is used for denoising. It leverages the difference in amplitude between spikes and noise in wavelet coefficients: Spikes have larger coefficients, while noise has smaller ones, enabling fine noise suppression.

First, select a wavelet basis adapted to spikes' characteristics and decompose $u_n(t)$ into L layers of wavelet coefficients

$$u_n(t) = A_L(t) + \sum_{l=1}^{L} D_l(t), \tag{2.21}$$

where $A_L(t)$ is the low-frequency approximation coefficient of the layer L containing main spike features, and $D_l(t)$ is the high-frequency detail coefficient of the layer l dominated by noise.

We then apply soft thresholding to the high-frequency detail coefficients. The threshold function is

$$\tilde{D}_l(t) = \begin{cases} \text{sign}(D_l(t)) \cdot (|D_l(t)| - \xi), & |D_l(t)| > \xi; \\ 0, & |D_l(t)| \le \xi. \end{cases} \tag{2.22}$$

The threshold ξ is determined by Stein's unbiased risk estimate (SURE)

$$\xi = \sigma \sqrt{2 \ln N}. \tag{2.23}$$

Here, we estimate the standard deviation σ of noise from the median of the first-layer high-frequency detail coefficients

$$\sigma = \frac{\text{median}(|D_1(t)|)}{0.6745}. \tag{2.24}$$

Next, we perform the inverse discrete wavelet transform (IDWT) to reconstruct the denoised noise component

$$\tilde{u}_n(t) = W^{-1}\left[A_L(t), \{\tilde{D}_l(t)\}_{l=1}^{L}\right]. \tag{2.25}$$

Finally, the denoised noise-dominant components are combined with the spike-dominant IMF components to obtain the final denoised and reconstructed neuronal spike signal.

3. Proposed denoising method

The proposed signal denoising framework based on self-optimizing VMD and wavelet thresholding is illustrated in Figure 1, with the detailed implementation steps outlined below

Step 1: Collect the raw extracellular neuronal recording signal $x(t)$.

Step 2: Regard envelope entropy as the objective fitness metric, and utilize the TOC algorithm to adaptively optimize the critical parameters of VMD, yielding the optimal mode count K and quadratic penalty factor α.

Step 3: Perform VMD decomposition on the raw noisy signal with the optimal K and α to obtain K intrinsic mode components $\{u_k\}$.

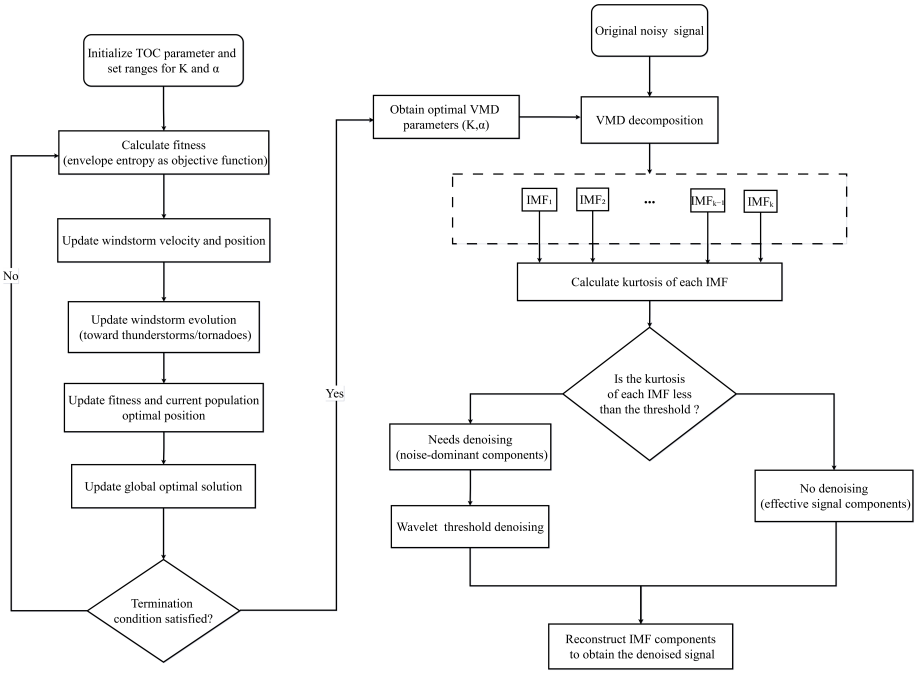

Figure 1. Flowchart of the proposed denoising framework based on TOC-optimized VMD and wavelet thresholding.

Step 4: Classify the $\{u_k\}$ components into effective components and noise-dominant components using the kurtosis criterion, then denoise the noise-dominant components by wavelet thresholding

(1) Calculate the kurtosis of each IMF component using Eq (3.1)

$$\text{Kurt} = \frac{\mathbb{E}\left[(x-\mu)^4\right]}{(\sigma^2)^2} = \frac{\frac{1}{N}\sum_{i=1}^{N}(x_i-\mu)^4}{\left(\frac{1}{N}\sum_{i=1}^{N}(x_i-\mu)^2\right)^2}, \tag{3.1}$$

where x_i is the original spike signal, μ is the mean value, σ^2 is the variance, and $\mathbb{E}[\cdot]$ is the mathematical expectation. The kurtosis of neuronal spike signals is much larger than 4, while the kurtosis of Gaussian noise is about 4, so $K_0 = 4$ is taken as the threshold value [32].

(2) Compare the kurtosis of each mode component with K_0: The components with $K_i \geq K_0$ are classified as effective components $\{u_{m_1}, u_{m_2}, \ldots, u_{m_p}\}$; the components with $K_i < K_0$ are sorted in descending order of kurtosis to form noise-dominant components $\{u_{n_1}, u_{n_2}, \ldots, u_{n_q}\}$.

(3) If the noise-dominant component set $\{u_{n_1}, u_{n_2}, \ldots, u_{n_q}\}$ contains only one component, it is directly removed; if it contains two or more components, the component u_{n_q} with the smallest kurtosis (the weakest correlation with the original signal, usually pure noise) is first removed, reducing the set to $\{u_{n_1}, u_{n_2}, \ldots, u_{n(q-1)}\}$, and then the wavelet threshold method in Section 2.4 is used to denoise this part of the components.

Step 5: Reconstruct the final denoised signal by superimposing the effective signal-dominant component set and the denoised noise-dominant component set. The reconstruction formula is

$$x'(t) = \sum_{i=1}^{p} u_{m_i}(t) + \sum_{j=1}^{q-1} \tilde{u}_{n_j}(t), \tag{3.2}$$

where p denotes the count of valid signal-dominant components, q represents the quantity of initial noise-dominant components, $x(t)$ corresponds to the raw noisy neuronal spike recording, while $x'(t)$ denotes the resulting denoised signal.

4. Experimental results

Experimental data: Both simulated and real data were used to verify the performance of the proposed denoising method.

(1) **Synthesized extracellular recording signals:** The simulated signals constructed in the experiment were obtained by superimposing spike trains generated from five different waveform templates with composite background noise. A Poisson process containing a refractory period was introduced into the spike trains to simulate the actual firing patterns of neurons. The composite background noise was composed of Gaussian white noise and real neuronal background noise. This construction method could adequately simulate the actual noise environment of electrophysiological recordings [33], and the specific signal forms are shown in Figure 2.

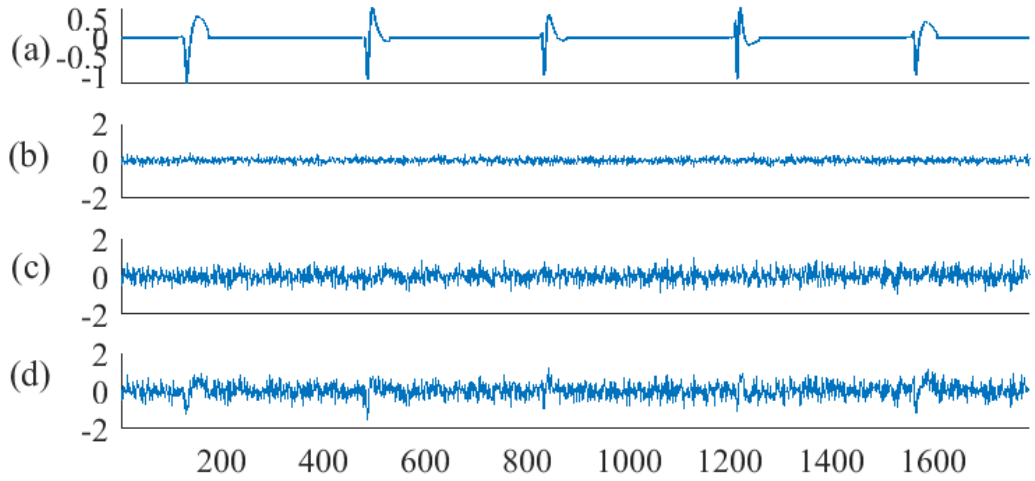

Figure 2. Synthesis process of neuronal spike signals: (a) Clean neuronal spike signal; (b) neural background noise; (c) Gaussian white noise; (d) synthesized noisy signal.

To comprehensively evaluate denoising performance across different noise levels, we generated simulated neuronal spike signals at four noise levels (NLs; 0.05, 0.10, 0.15, 0.20), as shown in Figure 3. These signals provide a series of challenging test scenarios to fully validate the robustness of the proposed method.

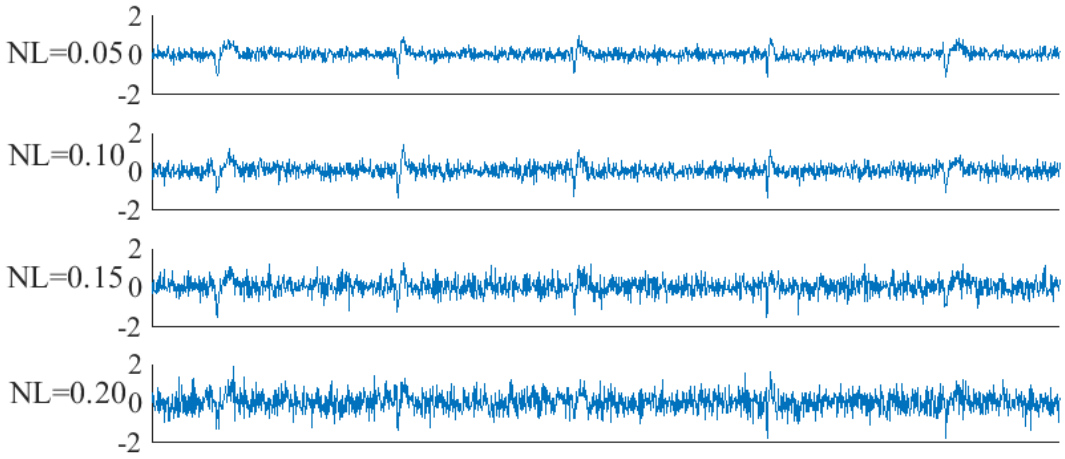

Figure 3. Simulated neuronal spike signals at different noise levels.

(2) **Real data:** The real neuronal signal used in the experiment was an extracellular recording signal from the prefrontal cortex of Long-Evans rats. The data were collected by the Shanghai Institute of Life Sciences, Chinese Academy of Sciences, in strict compliance with the ethical guidelines for animal experimentation. The original signal had a sampling rate of 40 kHz and was preprocessed with a 250-Hz high-pass filter to remove low-frequency drift interference while preserving spike and high-frequency neural activity components.

Evaluation criteria: To comprehensively and quantitatively assess the noise suppression effectiveness of different methods, five metrics are adopted: Signal-to-noise ratio (SNR), root mean square error (RMSE), mean absolute error (MAE), normalized cross-correlation (NCC), and energy signal-to-noise ratio (ESN) [34]. Their formulas are as follows

SNR:

$$\mathrm{SNR} = 10\lg\left(\frac{\sum_{i=1}^{N} x(t)^2}{\sum_{i=1}^{N}(x(t)-x'(t))^2}\right), \tag{4.1}$$

where N represents the total number of time samples, $x(t)$ corresponds to the raw noisy neuronal spike recording, and $x'(t)$ denotes the processed denoised signal. A higher SNR value indicates superior noise suppression performance.

RMSE:

$$\mathrm{RMSE} = \sqrt{\frac{1}{N}\sum_{i=1}^{N}(x(t)-x'(t))^2}. \tag{4.2}$$

A smaller RMSE indicates better denoising performance.

MAE:

$$\mathrm{MAE} = \frac{1}{N}\sum_{i=1}^{N}\left|x(t)-x'(t)\right|. \tag{4.3}$$

A smaller MAE indicates better denoising performance.

NCC:

$$\mathrm{NCC} = \frac{\sum_{i=1}^{N} x(t)x'(t)}{\sqrt{\left(\sum_{i=1}^{N} x(t)^2\right)\left(\sum_{i=1}^{N} x'(t)^2\right)}}. \tag{4.4}$$

A larger NCC indicates better denoising performance.

ESN:

$$\mathrm{ESN} = \frac{E'}{E} = \frac{\sum_{i=1}^{N}|x'(t)|^2}{\sum_{i=1}^{N}|x(t)|^2}, \tag{4.5}$$

where E is the energy of the original noisy signal, and E' is the energy of the denoised signal. A larger ESN indicates less energy loss and better denoising performance.

4.1. Simulated experiment

4.1.1. Parameter settings

In this work, TOC is used to adaptively optimize the key VMD parameters. The population size and maximum number of iterations for TOC are both set to 10, balancing convergence speed and optimization accuracy while avoiding excessive computational overhead. Other internal parameters follow the recommended configurations in the original literature [30]. The search range for the VMD mode number K is set to [2, 10] on the basis of the inherent characteristics of neuronal spike signals, while the quadratic penalty factor α is constrained to [100, 5000], a commonly adopted range in electrophysiological signal processing. The envelope entropy is used as the objective function to guide optimization, as it effectively quantifies the randomness of decomposed components and facilitates the separation of deterministic spikes from noise.

As illustrated by the TOC optimization curve in Figure 4, the algorithm converges to the minimum envelope entropy value of 6.7094 at the fourth iteration. Accordingly, the optimal VMD parameters are identified as $K^* = 8$ and $\alpha^* = 3367$, verifying that TOC has faster convergence and stronger stability than PSO in VMD parameter optimization.

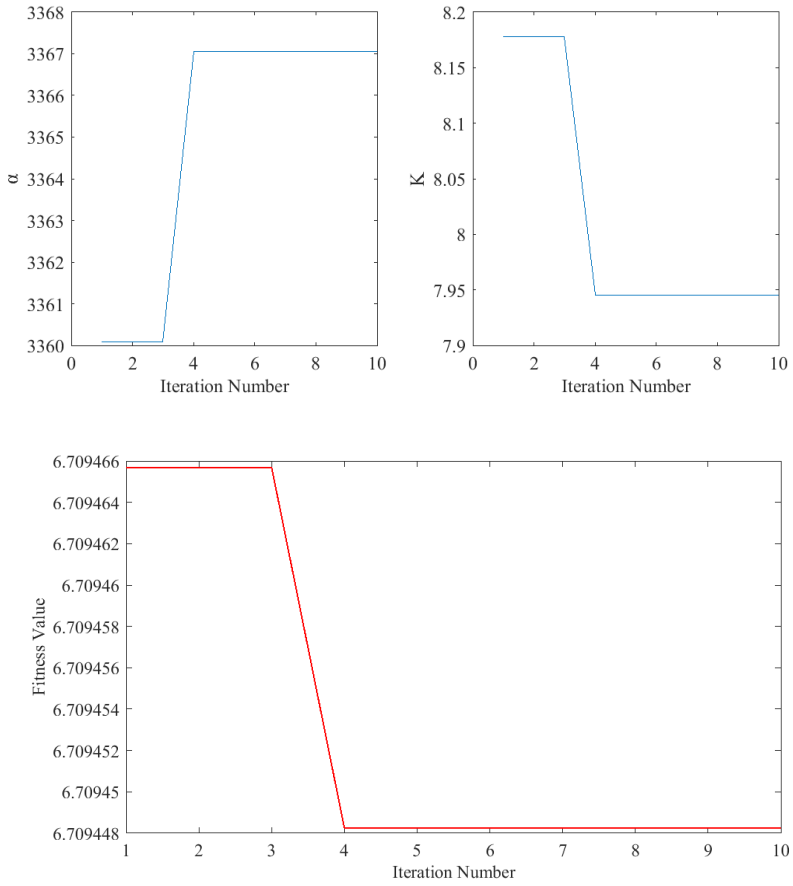

Figure 4. VMD parameter optimization convergence curve of TOC algorithm for simulated signals.

To analyze the influence of key VMD parameters on denoising performance, a parameter sensitivity analysis is conducted at the noise level of 0.10. Table 1 lists the denoising results for different mode numbers K with the penalty factor $\alpha = 3367$ being fixed. As K increases from 4 to 16, SNR, NCC, and ESN increase gradually and tend to stabilize, while RMSE and MAE decrease gradually and tend to stabilize. This indicates that a larger K helps achieve a finer decomposition and better separation between neural spikes and noise. Figure 5 shows the corresponding variation curves from Table 1, which intuitively illustrate the trends of these indicators with K. The red-marked point $K^* = 8$ in the figure is the optimal mode number determined by the TOC algorithm.

Table 1. Effect of mode number K on denoising performance for simulated signals.

K	SNR/dB	RMSE	MAE	NCC	ESN
4	7.2257	0.0765	0.1059	0.9046	66.72%
6	9.8714	0.0620	0.0780	0.9487	76.00%
7	11.3000	0.0550	0.0730	0.9557	78.00%
8	12.5065	0.0501	0.0634	0.9673	81.15%
9	12.6349	0.0461	0.0631	0.9681	82.25%
10	12.9795	0.0452	0.0629	0.9685	82.37%
11	13.2411	0.0434	0.0612	0.9712	83.31%
12	13.3736	0.0427	0.0586	0.9741	83.45%
14	13.4812	0.0417	0.0575	0.9763	83.57%
16	13.5950	0.0392	0.0559	0.9771	84.01%

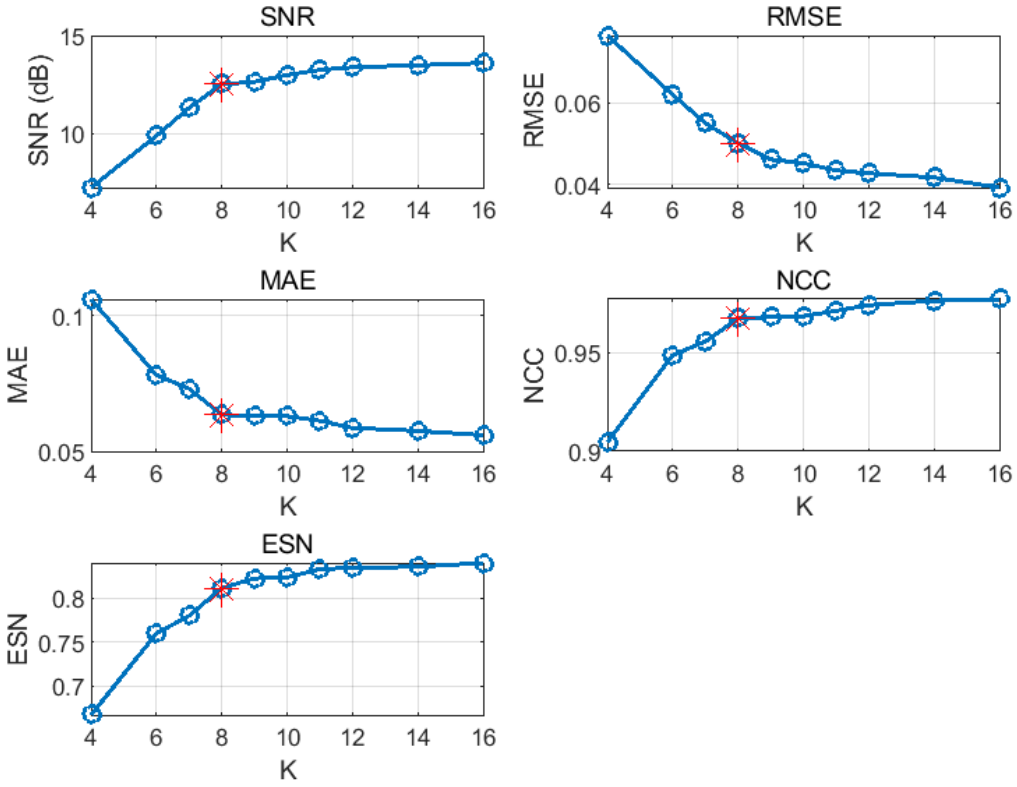

Figure 5. Parameter sensitivity analysis curves of the mode number K on denoising performance for simulated signals.

Table 2 shows the denoising performance for different penalty factors α with the optimal mode number $K = 8$ being fixed. As α gradually increases from 1000 to 5000, SNR, NCC, and ESN decrease gradually, while RMSE and MAE increase gradually. This trend is the opposite of that for increasing values of K. A larger α strengthens the bandwidth constraint, potentially excessively suppressing

the effective components of spike signals and reducing the denoising effect. Figure 6 displays the corresponding variation curves, where performance declines gradually with increasing α. The red-marked point $\alpha^* = 3367$ in the figure is the optimal penalty factor obtained by the TOC algorithm.

Table 2. Effect of penalty factor α on denoising performance for simulated signals.

α	SNR/dB	RMSE	MAE	NCC	ESN
1000	13.2620	0.0423	0.0529	0.9772	86.66%
1500	12.3706	0.0467	0.0586	0.9722	85.11%
2000	12.2012	0.0469	0.0597	0.9713	84.97%
2500	11.5285	0.0481	0.0646	0.9673	83.27%
3000	10.7911	0.0519	0.0703	0.9605	81.85%
3367	9.4065	0.0611	0.0824	0.9436	75.61%
3800	9.1748	0.0627	0.0846	0.9404	75.28%
4000	9.0793	0.0633	0.0856	0.9390	74.91%
4500	8.8651	0.0648	0.0877	0.9359	74.53%
5000	8.6786	0.0661	0.0896	0.9330	73.23%

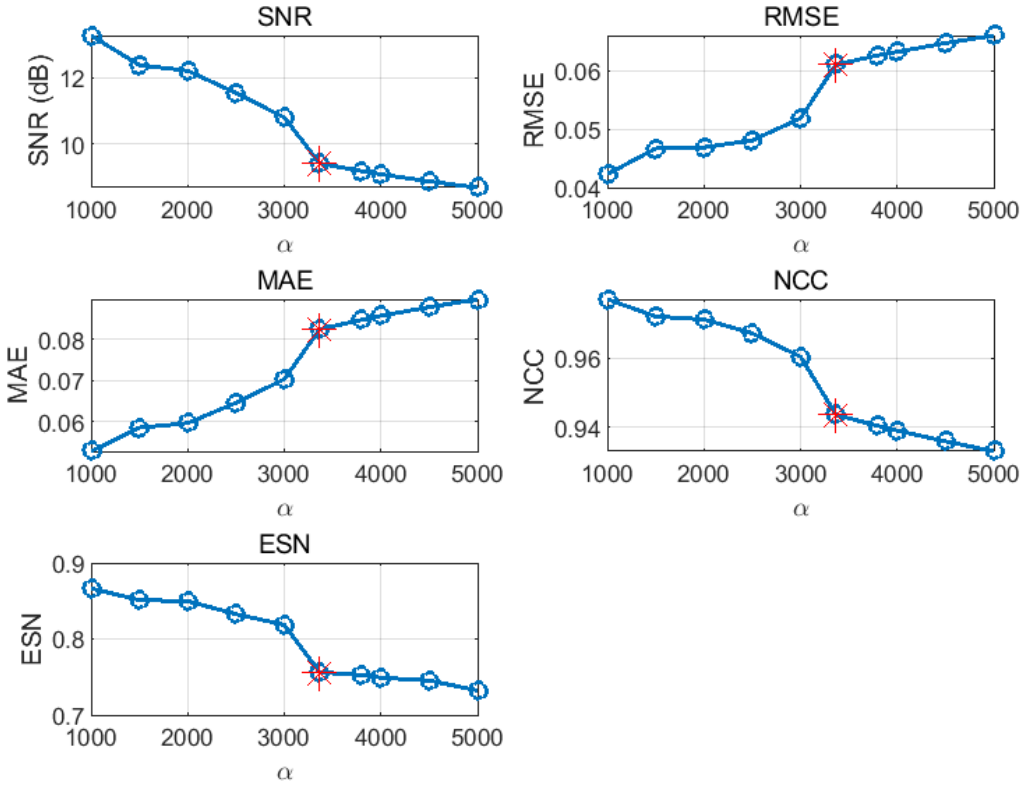

Figure 6. Parameter sensitivity analysis curves of penalty factor α on denoising performance for simulated signals.

In summary, K and α show opposite trends in their influence on denoising performance. Increasing K improves the decomposition fineness, while increasing α strengthens the bandwidth constraint. A reasonable trade-off between the two parameters is necessary to achieve the best denoising performance. The optimal parameter combination $K^* = 8$ and $\alpha^* = 3367$ obtained by the TOC algorithm achieves a good balance of decomposition adequacy, signal preservation, and noise suppression.

With the optimal parameters, the TOC-VMD decomposition was performed on the simulated signal to obtain eight IMF components distributed from high frequency to low frequency. The specific decomposition results are shown in Figure 7.

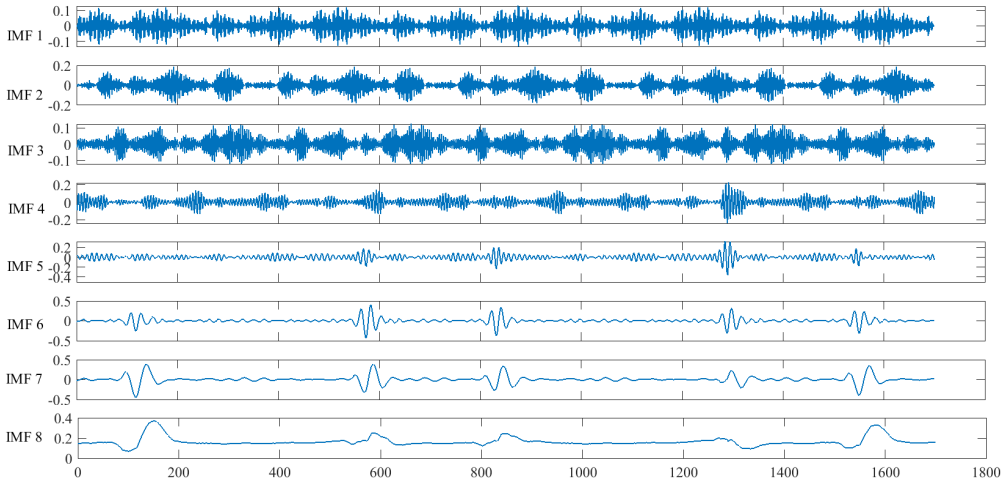

Figure 7. TOC-VMD frequency-domain decomposition results for simulated signals.

4.1.2. Denoising performance analysis

To investigate how different mode selection criteria influence the final noise suppression outcome, the experiment calculated five characteristic indicators for each IMF component: Correlation coefficient, sample entropy, envelope entropy, kurtosis, and spectral kurtosis. The specific values are shown in Table 3.

Table 3. Characteristic indicators of IMF from the TOC-VMD decomposition of simulated signals.

	R	Sample entropy	Envelope entropy	Kurtosis	Spectral kurtosis
IMF1	0.2243	0.4040	10.4747	3.0380	2.2223
IMF2	0.2408	0.1016	10.5491	2.7897	2.4730
IMF3	0.2343	0.1833	10.4873	4.3200	2.6259
IMF4	0.2974	0.3136	10.4509	6.0841	3.0099
IMF5	0.3798	0.1433	10.0971	10.3480	4.0135
IMF6	0.5031	0.0783	9.9028	10.5515	4.2843
IMF7	0.5999	0.0504	9.6860	9.7610	2.6987
IMF8	0.3808	0.0120	10.6887	9.1373	2.9679

We select effective components and reconstruct denoised signals based on different criteria. The correlation coefficient method selects components with $R > 0.5$ (IMF6 and IMF7), but it may miss useful neural components, such as IMF5. The sample entropy method focuses on components with low complexity (IMF2, IMF7, and IMF8), while the envelope entropy method tends to select components with concentrated energy (IMF5, IMF6, and IMF7). The reconstructed waveforms under each screening rule are shown in Figure 8. However, these methods cannot accurately identify transient spike components. The spectral kurtosis values of different components are close, making it difficult to distinguish signals from noise. The kurtosis criterion performs best. By setting the kurtosis threshold to 4, we select components with obvious spike characteristics, namely IMF3–IMF8. This criterion effectively highlights the transient impulse characteristics of neuronal spikes and accurately separates signal-dominant components from noise-dominant components.

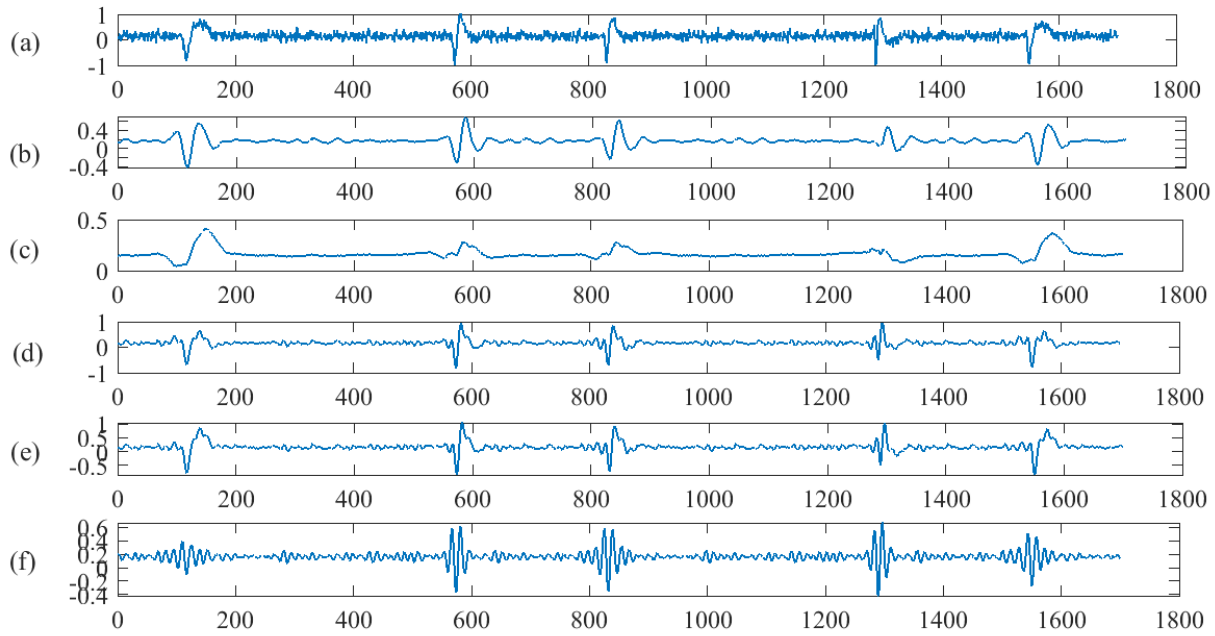

Figure 8. Comparison of simulated signal reconstruction results with different component screening criteria.

To avoid losing useful information in the spike signal and further improve denoising, wavelet soft thresholding is applied to the noise-dominant IMF components again. The simulated spike signal is a transient impulse with a rapid rise and fall. The db4 wavelet is widely recognized as suitable for capturing abrupt signals due to its compact support and good time-frequency localization. Thus, we choose the db4 wavelet as the basis function [35]. The decomposition level is set to 4 after experimental testing, which balances noise suppression and detail preservation. We can combine the effective IMF components and the denoised components to obtain the final denoised signal, as shown in Figure 9. It can be seen that the signal information is well preserved, the waveform distortion is reduced, and the kurtosis-based method combined with wavelet thresholding achieves the best reconstruction performance.

We conduct a quantitative analysis to compare different reconstruction methods and summarize the results in Table 4. The data show that the kurtosis-based component selection method performs well across all five evaluation metrics. Among all tested strategies, it achieves the highest SNR of 9.7076 dB, along with the lowest MAE of 0.0615 and RMSE of 0.0720. It also obtains the highest NCC of 0.9576 and the highest ESN of 88.36%. Other criteria, such as R, sample entropy, envelope entropy, and spectral kurtosis, show lower SNR, NCC, and ESN values, along with higher MAE and RMSE. The kurtosis-based method, therefore, effectively balances noise suppression and signal detail preservation. It reduces noise while preserving the key morphological and temporal features of spikes.

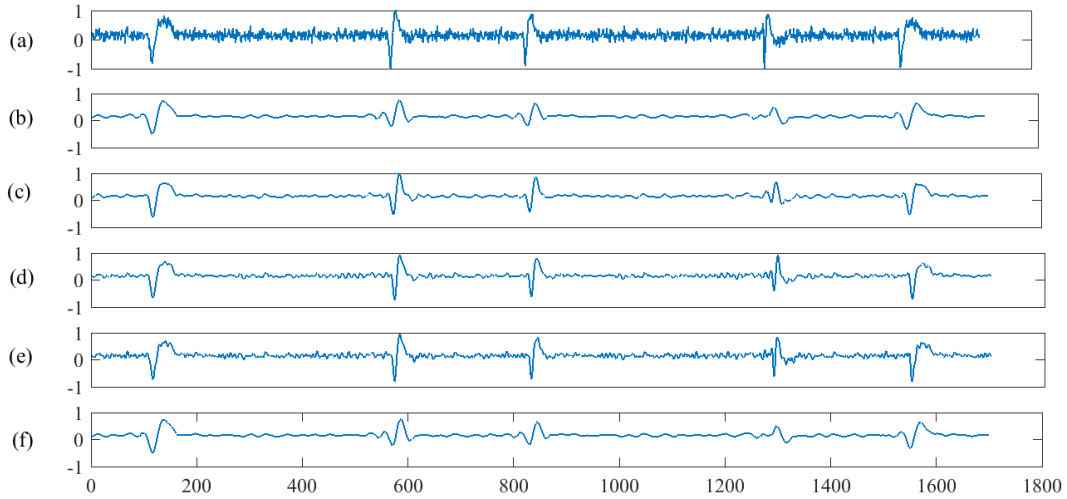

Figure 9. Reconstruction results of simulated signals with different component screening criteria after wavelet threshold optimization.

Table 4. Comparison of denoising performance indicators of simulated signals with different component screening criteria.

	R	Sample entropy	Envelope entropy	Kurtosis	Spectral kurtosis
SNR/dB	3.4807	5.3254	6.7918	9.7076	4.0590
MAE	0.0980	0.0963	0.0806	0.0615	0.0948
RMSE	0.1359	0.1298	0.1032	0.0720	0.1268
NCC	0.8360	0.8520	0.9091	0.9576	0.8600
ESN	67.15%	67.89%	78.74%	88.36%	70.41%

To further evaluate the performance of the proposed method, we compare the TOC-VMD-wavelet threshold method with three denoising methods: Classic EMD [36], conventional VMD [37], and PSO-VMD [38]. The EMD method does not require predefined decomposition parameters and can adaptively decompose the signal. For the standard VMD method, we set the quadratic penalty factor as $\alpha = 3000$ and the number of modes as $K = 4$, based on experience. For the PSO-VMD method, we use PSO to automatically adjust these key parameters. To make the comparison fair, all three decomposition-based methods use the same kurtosis threshold of 4 to select effective

components for signal reconstruction. To ensure the statistical reliability of the results, all denoising performance indicators (SNR, MAE, RMSE, NCC, and ESN) are averaged across 20 independent repeated experiments at each noise level, thereby reducing the influence of random errors in a single trial. We compare the performance of different denoising methods under four noise levels and present the results in Table 5.

Table 5. Comparison of the denoising performance indicators of simulated signals with different denoising methods.

Noise level	Method	SNR/dB	MAE	RMSE	NCC	ESN
0.05	TOC-VMD-wavelet	14.7670	0.0329	0.0472	0.9810	88.37%
	PSO-VMD	12.3427	0.0468	0.0567	0.9524	80.12%
	VMD	8.5435	0.0533	0.0878	0.9309	72.34%
	EMD	4.0302	0.1461	0.1445	0.7808	62.35%
0.10	TOC-VMD-wavelet	9.7620	0.0615	0.0826	0.9625	79.25%
	PSO-VMD	8.0721	0.0752	0.0943	0.9317	72.64%
	VMD	5.9927	0.0915	0.1221	0.8682	61.78%
	EMD	3.1638	0.1557	0.1790	0.6773	55.54%
0.15	TOC-VMD-wavelet	7.6536	0.0872	0.1125	0.9314	71.36%
	PSO-VMD	6.1245	0.1036	0.1287	0.8926	64.28%
	VMD	3.0430	0.1320	0.1672	0.7188	51.36%
	EMD	2.8142	0.1687	0.2042	0.6223	43.25%
0.20	TOC-VMD-wavelet	5.6247	0.1153	0.1462	0.8927	63.25%
	PSO-VMD	4.0126	0.1342	0.1675	0.8413	56.17%
	VMD	2.4373	0.1503	0.1880	0.6630	42.07%
	EMD	1.2355	0.1868	0.2294	0.5301	38.46%

The proposed TOC-VMD-wavelet method consistently outperforms the other tested denoising methods. At all noise levels, it achieves a higher SNR than PSO-VMD, VMD, and EMD, paired with lower MAE and RMSE, indicating smaller signal reconstruction errors. It also maintains higher NCC and ESN values, reflecting stronger correlation with the original signal and more effective preservation of spike features. For instance, at the 0.05 noise level, the proposed method achieves an SNR of 14.7670 dB, an MAE of 0.0329, an RMSE of 0.0472, an NCC of 0.9810, and an ESN of 88.37%. Even at the 0.20 noise level, its SNR remains 5.6247 dB, still higher than all other methods, while the MAE and RMSE are 0.1153 and 0.1462, respectively, both lower than those of other methods under the same condition. Across all noise levels, EMD shows the lowest SNR and the highest MAE and RMSE. PSO-VMD outperforms standard VMD and EMD but still lags behind the proposed method in most indicators. Overall, the proposed method balances noise suppression and signal fidelity more effectively than the other methods, achieving effective noise reduction while preserving the key spike features even at high noise levels.

Since both the proposed TOC-VMD-wavelet method and the PSO-VMD method adopt intelligent optimization algorithms, their results are subject to random fluctuations. A simple comparison based on mean values alone cannot fully demonstrate that the proposed method's performance improvement is statistically significant. Therefore, statistical verification is conducted in this paper. To further confirm

the reliability of the performance differences between the two methods, Welch's two-sample t-test is used, based on 20 independent repeated experiments at each noise level.

Welch's t-test is an improved version of the independent-samples t-test, suitable for comparing the means of two groups with unequal variances regardless of sample sizes. It can provide more reliable p-values under heterogeneous variance conditions [39].

The statistical results of the mean and standard deviation of each denoising index for the two methods under different noise levels are shown in Table 6. It can be seen from Table 6 that, in terms of SNR, RMSE, MAE, NCC, and ESN, the proposed method achieves better mean values under all four noise levels, and the overall standard deviation is smaller than that of the PSO-VMD method, indicating that the proposed method not only delivers better denoising performance but also yields more stable and reliable results.

Table 6. Descriptive statistics of simulation signal denoising performance.

Noise level	Index	TOC-VMD-wavelet (mean ± std)	PSO-VMD (mean ± std)
0.05	SNR/dB	14.7670 ± 2.6015	12.3427 ± 3.1247
0.05	MAE	0.0329 ± 0.0082	0.0468 ± 0.0125
0.05	RMSE	0.0472 ± 0.0140	0.0567 ± 0.0187
0.05	NCC	0.9810 ± 0.0120	0.9524 ± 0.0165
0.05	ESN	88.37% ± 4.12%	80.12% ± 5.34%
0.10	SNR/dB	9.7620 ± 2.3375	8.0721 ± 2.8513
0.10	MAE	0.0615 ± 0.0114	0.0752 ± 0.0163
0.10	RMSE	0.0826 ± 0.0165	0.0943 ± 0.0211
0.10	NCC	0.9625 ± 0.0156	0.9317 ± 0.0204
0.10	ESN	79.25% ± 4.53%	72.64% ± 5.16%
0.15	SNR/dB	7.6536 ± 2.1024	6.1245 ± 2.6318
0.15	MAE	0.0872 ± 0.0152	0.1036 ± 0.0201
0.15	RMSE	0.1125 ± 0.0203	0.1287 ± 0.0254
0.15	NCC	0.9314 ± 0.0187	0.8926 ± 0.0245
0.15	ESN	71.36% ± 4.82%	64.28% ± 5.63%
0.20	SNR/dB	5.6247 ± 1.8736	4.0126 ± 2.3542
0.20	MAE	0.1153 ± 0.0186	0.1342 ± 0.0235
0.20	RMSE	0.1462 ± 0.0241	0.1675 ± 0.0296
0.20	NCC	0.8927 ± 0.0215	0.8413 ± 0.0286
0.20	ESN	63.25% ± 5.14%	56.17% ± 6.02%

For two independent sets of denoising indicators, let $\bar{x}_1$ and $\bar{x}_2$ denote the mean values of the TOC-VMD-wavelet method and the PSO-VMD method, s_1 and s_2 denote their respective standard deviations, and $n_1 = n_2 = 20$ denote the number of repeated experiments for each group. The t-statistic is calculated as follows [40]:

$$t = \frac{\bar{x}_1 - \bar{x}_2}{\sqrt{\frac{s_1^2}{n_1} + \frac{s_2^2}{n_2}}}, \tag{4.6}$$

and the degrees of freedom are corrected using the Welch–Satterthwaite equation:

$$df = \frac{\left(\frac{s_1^2}{n_1} + \frac{s_2^2}{n_2}\right)^2}{\frac{(s_1^2/n_1)^2}{n_1-1} + \frac{(s_2^2/n_2)^2}{n_2-1}}. \tag{4.7}$$

According to this, the two-tailed p-value is calculated. In this study, $p < 0.05$ is defined as indicating a statistically significant difference in denoising performance between the two methods, which is marked with the symbol "*".

Table 7 presents the statistical test results under four noise levels. At all noise levels, the degrees of freedom (df) are sufficient to ensure the validity of the test, and the t-values of all indicators are consistent with the expected direction of performance improvement, confirming that the proposed TOC-VMD-wavelet method outperforms PSO-VMD in most denoising indicators. Specifically, the differences in the key metrics, including SNR, MAE, NCC, and ESN, are statistically significant (marked with an asterisk, $p < 0.05$) under nearly all noise conditions, while only the RMSE metric at noise levels of 0.05 and 0.10 yields $p > 0.05$; however, even in these cases, the proposed method still exhibits better mean values, showing a consistent performance advantage. These results indicate that the superiority of the proposed method is not due to random factors but is statistically robust. Combined with the standard deviation data in Table 6, the smaller overall standard deviation of the proposed method indicates that its performance is more stable and reliable than that of PSO-VMD, thereby verifying the method's effectiveness and robustness from a quantitative perspective.

Table 7. Significance test results for simulation signal denoising.

Noise level	Index	t	df	p
0.05	SNR	2.6665	36.7917	0.0113*
0.05	MAE	-4.1582	32.7976	0.0002*
0.05	RMSE	-1.8187	35.2073	0.0775
0.05	NCC	6.2691	34.7054	0.0000*
0.05	ESN	5.4703	35.7019	0.0000*
0.10	SNR	2.0498	36.5926	0.0476*
0.10	MAE	-3.0802	33.9988	0.0041*
0.10	RMSE	-1.9534	35.9129	0.0586
0.10	NCC	5.3635	35.5589	0.0000*
0.10	ESN	4.3052	37.3734	0.0001*
0.15	SNR	2.0301	36.2322	0.0497*
0.15	MAE	-2.9104	35.3756	0.0062*
0.15	RMSE	-2.2281	36.2389	0.0322*
0.15	NCC	5.6299	35.5282	0.0000*
0.15	ESN	4.2721	37.1186	0.0001*
0.20	SNR	2.3962	36.1774	0.0219*
0.20	MAE	-2.8203	36.0960	0.0077*
0.20	RMSE	-2.4956	36.5001	0.0172*
0.20	NCC	6.4245	35.2766	0.0000*
0.20	ESN	3.9999	37.0889	0.0003*

*$p < 0.05$, significant difference

We further compare the running time of different denoising methods to evaluate their computational efficiency. The results are presented in Table 8, where the values represent the average running time over four noise levels for simulated signals.

Table 8. Running time comparison of different denoising methods for simulated signals.

Method	Running time (s)
PSO-VMD	31.1216
TOC-VMD-wavelet	16.0621
VMD	5.6840
EMD	0.3218

The EMD method takes the shortest time of 0.3218 seconds, thanks to its simple adaptive decomposition and lack of complex optimization. The traditional VMD method takes 5.6840 seconds, as it uses fixed parameters and requires no iterative optimization, achieving high efficiency. The PSO-VMD method takes the longest time of 31.1216 seconds, mainly because the PSO converges slowly and needs extensive iterations, increasing the computational complexity.

The proposed TOC-VMD-wavelet method takes 16.0621 seconds, longer than EMD and VMD. This trade-off comes from parameter optimization and wavelet denoising, which improve the denoising performance. Though not the fastest, it outperforms EMD/VMD in denoising accuracy and spike retention, and is more efficient than PSO-VMD. Overall, it achieves a balanced trade-off among denoising performance, feature retention, and computational efficiency.

4.2. Real experiment

4.2.1. Parameter settings

The experiment kept the TOC algorithm's parameter settings consistent with those in the simulation experiment and performed an adaptive optimization of VMD parameters for the real signal. The optimization curve in Figure 10 shows that the algorithm converged stably after the fifth iteration and ultimately reached the minimum envelope entropy of 12.3167. The corresponding optimal VMD parameters were the mode number $K^* = 7$ and the quadratic penalty factor $\alpha^* = 3538$. This result again verifies that the TOC algorithm has efficient adaptive optimization ability.

To further verify the parameter sensitivity law on real signals, we analyzed the effects of K and α on denoising performance. As shown in Table 9, Figure 11, Table 10, and Figure 12, the variation trends are completely consistent with those of the simulated signals: The denoising performance improves rapidly with increasing K and then stabilizes, while it gradually decreases with increasing α. Such consistent variation laws further verify the rationality of selecting the optimal parameter combination $K^* = 7$, $\alpha^* = 3538$ determined by the TOC algorithm for real neuronal spike denoising.

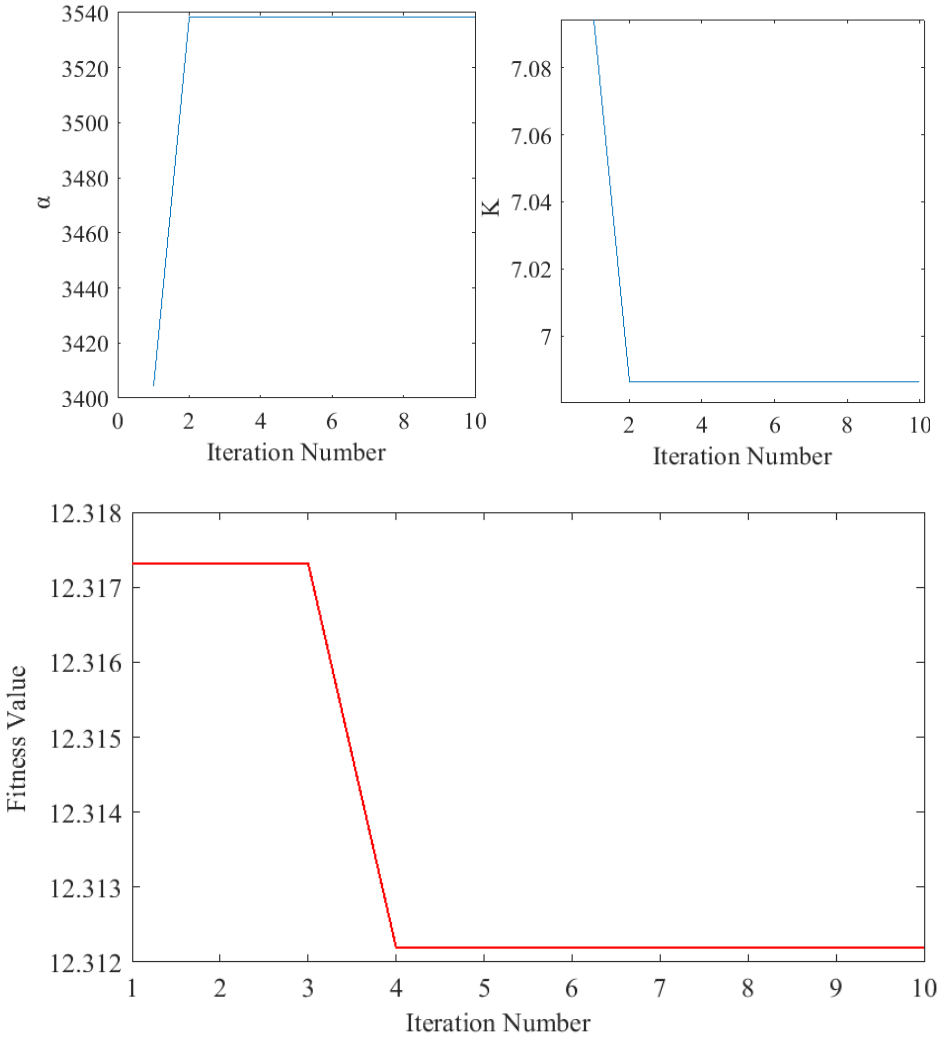

Figure 10. VMD parameter optimization convergence curve of the TOC algorithm for real signals.

Table 9. Effect of mode number K on denoising performance for real signals.

K	SNR/dB	RMSE	MAE	NCC	ESN
4	20.1172	0.0412	0.0538	0.9923	96.14%
6	22.8501	0.0307	0.0393	0.9959	97.36%
7	23.8715	0.0251	0.0333	0.9971	97.86%
8	23.9731	0.0246	0.0328	0.9972	97.91%
9	23.9942	0.0229	0.0293	0.9977	97.97%
10	24.0575	0.0223	0.0288	0.9978	97.99%
11	24.0973	0.0218	0.0282	0.9979	98.15%
12	24.1132	0.0213	0.0278	0.9980	98.25%
14	24.1978	0.0209	0.0274	0.9980	98.30%
16	24.2342	0.0204	0.0271	0.9980	98.42%

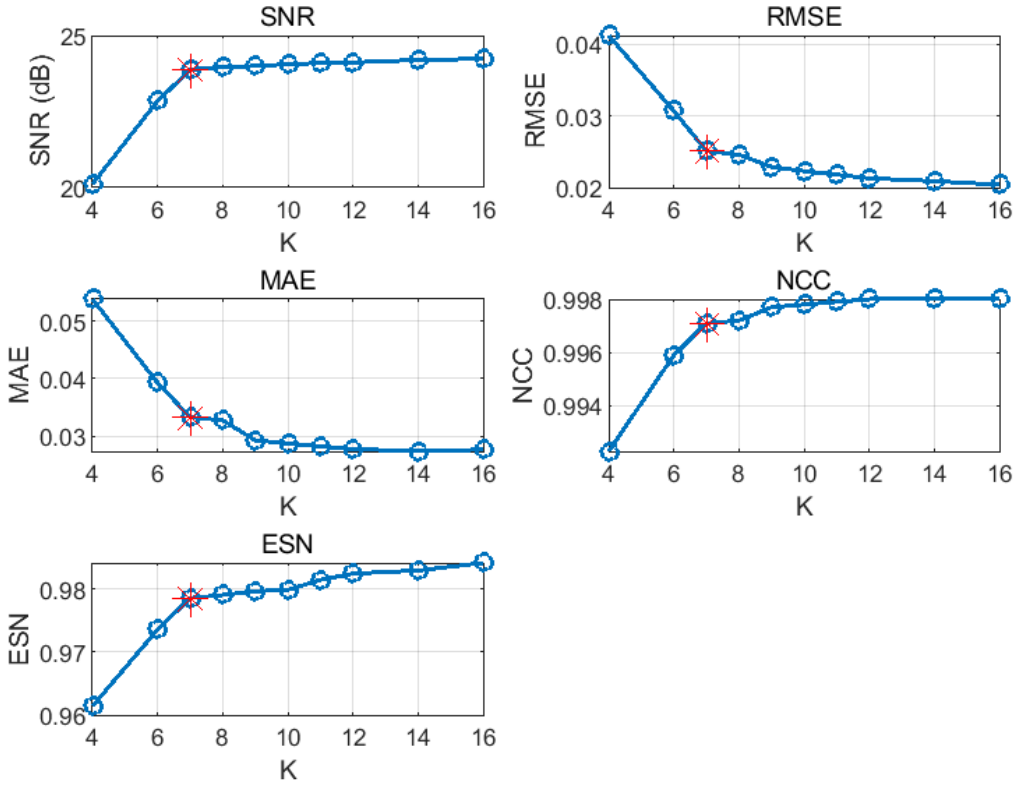

Figure 11. Parameter sensitivity analysis curves of the mode number K on denoising performance for real signals.

Table 10. Effect of penalty factor α on denoising performance for real signals.

α	SNR/dB	RMSE	MAE	NCC	ESN
1000	24.1519	0.0207	0.0268	0.9981	98.33%
1500	23.9000	0.0212	0.0273	0.9980	98.28%
2000	23.7407	0.0221	0.0281	0.9979	98.13%
2500	23.1229	0.0237	0.0302	0.9976	97.94%
3000	22.5980	0.0252	0.0321	0.9973	97.77%
3538	22.2715	0.0261	0.0333	0.9971	97.66%
3800	22.1000	0.0265	0.0338	0.9970	97.60%
4000	22.0000	0.0267	0.0340	0.9969	97.58%
4500	21.9500	0.0268	0.0341	0.9969	97.57%
5000	21.9000	0.0269	0.0342	0.9968	97.56%

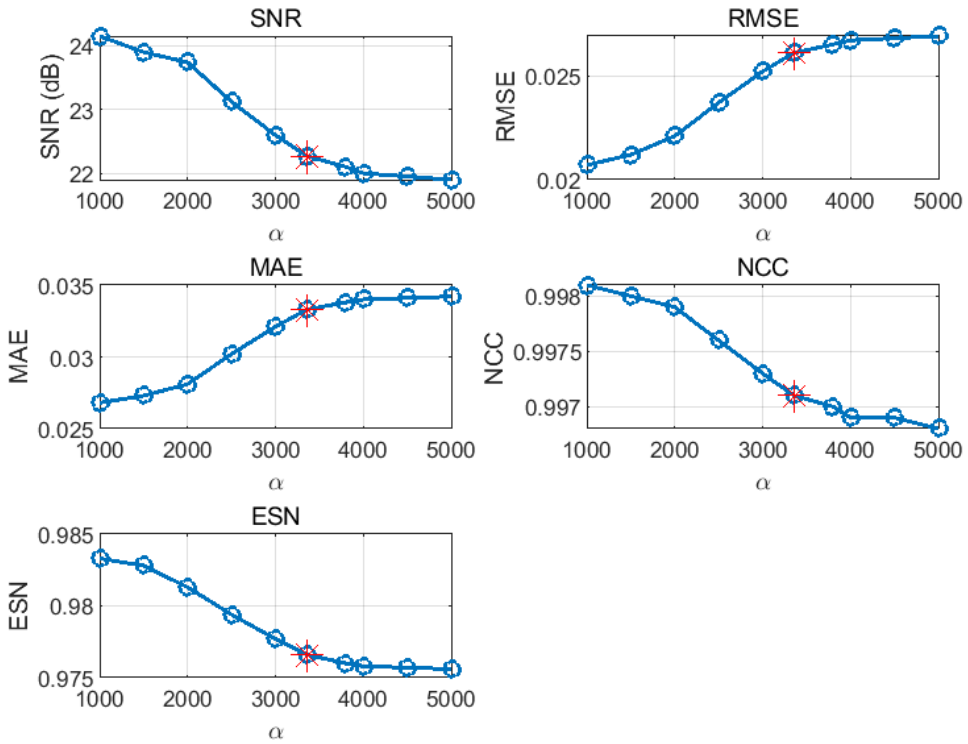

Figure 12. Parameter sensitivity analysis curves of the penalty factor α on denoising performance for real signals.

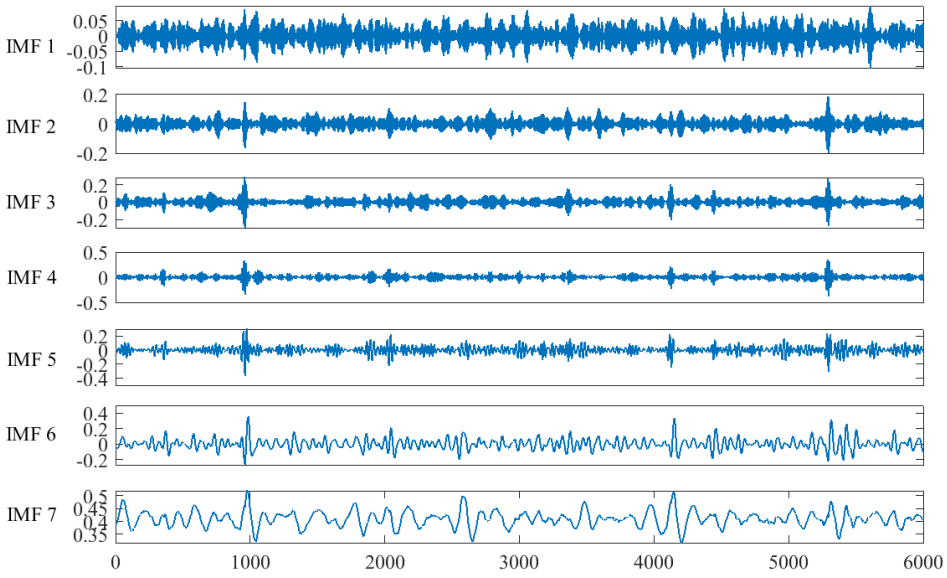

Figure 13. TOC-VMD frequency-domain decomposition results for real neuronal spike signals.

On the basis of these optimal parameters, we conducted TOC-VMD decomposition on the preprocessed real signals and obtained seven IMF components sorted from high frequency to low frequency, as illustrated in Figure 13. Each component exhibited a clear separation effect in the frequency domain.

4.2.2. Denoising performance analysis

To explore the impact of different mode selection criteria on the denoising performance, five indicators, including correlation coefficient, sample entropy, envelope entropy, kurtosis, and spectral kurtosis, were calculated for each IMF component to distinguish signal-dominant and noise-dominant components, with results summarized in Table 11.

Table 11. Characteristic indicators of IMF from the TOC-VMD decomposition of real signals

	R	Sample entropy	Envelope entropy	Kurtosis	Spectral kurtosis
IMF1	0.1762	0.0940	12.3402	2.9654	2.3836
IMF2	0.2402	0.2536	12.3511	3.1828	2.4086
IMF3	0.3350	0.3375	12.2920	7.7731	2.4294
IMF4	0.4550	0.3391	12.2312	12.7087	2.4778
IMF5	0.5652	0.3059	12.2318	7.5542	2.3383
IMF6	0.6750	0.1742	12.2561	5.4825	2.3296
IMF7	0.4594	0.0270	12.5468	3.8291	2.5687

Consistent with the simulation experiment, we adopt the same set of component screening rules for real signals. We select effective components and reconstruct denoised signals with different criteria. The correlation coefficient method selects components with $R > 0.5$ (IMF5 and IMF6), but it may miss useful neural components such as IMF4. The sample entropy method tends to select low-complexity components (IMF1 and IMF7), while the envelope entropy method prefers components with concentrated energy (IMF5–IMF7). However, these criteria cannot reliably identify transient spike components. Consistent with the simulation, the kurtosis criterion performs best. By setting the kurtosis threshold to 4, we select components with obvious spike characteristics (IMF3–IMF6). This criterion effectively highlights the transient impulse characteristics of neuronal spikes and accurately separates signal-dominant components from noise-dominant ones.

To avoid losing useful information in the real spike signal and further improve denoising, wavelet soft thresholding is applied to the noise-dominant IMF components again. The real spike signal contains more complex noise and transient components. The biorthogonal (bior) wavelet family, such as bior2.2, offers a good balance between smoothness and symmetry, making them suitable for processing real-world signals with strong background noise while preserving morphological features. Thus, we choose the bior2.2 wavelet as the basis function [18]. The decomposition level is set to 5 after experimental testing, which balances noise suppression and detail preservation. Then we combine the effective IMF components and the denoised components to get the final denoised signal. The kurtosis method combined with wavelet thresholding shows the best reconstruction performance in the subsequent quantitative analysis.

We conduct the quantitative analysis to compare different reconstruction methods and summarize

the results in Table 12. The data show that the kurtosis-based component selection method performs well across all five evaluation metrics. Among all tested strategies, it achieves the highest SNR of 26.1589 dB, along with the lowest MAE of 0.0169 and RMSE of 0.0213. It also obtains the highest NCC of 0.9988 and the highest ESN of 99.97%. Other criteria, such as R, sample entropy, envelope entropy, and spectral kurtosis, show lower SNR, NCC, and ESN values, along with higher MAE and RMSE. The kurtosis-based method, therefore, effectively balances noise suppression and signal detail preservation. It reduces noise while preserving the key morphological and temporal features of spikes.

Table 12. Comparison of denoising performance indicators of real signals with different component screening criteria.

	R	Sample entropy	Envelope entropy	Kurtosis	Spectral kurtosis
SNR/dB	15.7561	15.2228	21.8304	26.1589	17.1151
MAE	0.0520	0.0553	0.0281	0.0169	0.0454
RMSE	0.0696	0.0739	0.0356	0.0213	0.0597
NCC	0.9870	0.9853	0.9967	0.9988	0.9904
ESN	97.36%	97.14%	99.26%	99.97%	97.85%

To further verify the performance of the proposed method on real signals, we compare it with the three baseline methods used in the simulation experiments. The results are presented in Table 13, where all reported values are the averages of 20 independent repeated experiments.

As shown in Table 13, the four methods exhibit clear differences in denoising performance. EMD suffers from significant mode mixing and limited noise suppression, resulting in the worst overall denoising performance. Traditional VMD can avoid mode mixing, yet it relies on manually preset parameters and shows poor adaptability to real signals. Although PSO-VMD optimizes the parameters adaptively, it often falls into local optima, resulting in limited performance. The proposed TOC-VMD-Wavelet method achieves optimal results across all evaluation indicators, with an SNR of 24.2154 dB, an MAE of 0.0171, an RMSE of 0.0238, an NCC of 0.9946, and an ESN of 96.84%. Compared with PSO-VMD, which delivers the best comprehensive performance among the contrastive methods, the proposed method obtains a higher SNR and lower error indicators, along with improved signal correlation and energy retention. It can effectively eliminate complex noise in real signals while preserving the original waveform and energy features of neuronal spikes to the greatest extent.

Table 13. Comparison of denoising performance indicators of real signals with different denoising methods.

Method	SNR/dB	MAE	RMSE	NCC	ESN
TOC-VMD-wavelet	24.2154	0.0171	0.0238	0.9946	96.84%
PSO-VMD	19.7402	0.0285	0.0388	0.9914	95.71%
VMD	15.5930	0.0385	0.0501	0.9673	93.20%
EMD	10.1832	0.0986	0.1340	0.9452	90.54%

Consistent with the evaluation procedure adopted in simulation experiments, we conduct a statistical comparative analysis between the proposed TOC-VMD-wavelet method and the PSO-VMD method on real signals.

Table 14 summarizes the mean and standard deviation of each denoising index for the two methods based on 20 independent repeated experiments. In terms of the five core indicators, namely SNR, MAE, RMSE, NCC, and ESN, the proposed method achieves better mean values with distinctly lower standard deviations. This indicates that the proposed method not only delivers superior overall denoising performance but also produces less scattered results across repeated experiments, thereby possessing higher stability and robustness.

Table 14. Descriptive statistics of real signal denoising performance.

Index	TOC-VMD-wavelet (mean ± std)	PSO-VMD (mean ± std)
SNR/dB	24.2154 ± 2.4692	19.7402 ± 3.8215
MAE	0.0171 ± 0.0086	0.0285 ± 0.0206
RMSE	0.0238 ± 0.0115	0.0388 ± 0.0274
NCC	0.9946 ± 0.0028	0.9914 ± 0.0052
ESN	96.84% ± 1.13%	95.71% ± 2.05%

As shown in Table 15, the results of Welch's t-test indicate that all evaluation their indicators possess sufficient degrees of freedom to ensure valid statistical analysis, the obtained t-values are consistent with the expected performance improvement direction, and all corresponding p-values are lower than 0.05, which further verifies that the proposed method achieves statistically significant and stable performance superiority over the PSO-VMD method.

Table 15. Significance test results for real signal denoising.

Index	t	df	p
SNR	4.3988	32.5098	0.0001*
MAE	-2.2838	25.4276	0.0310*
RMSE	-2.2575	25.4924	0.0328*
NCC	2.4231	29.1634	0.0218*
ESN	2.1589	29.5702	0.0391*

*$p < 0.05$, significant difference

We further compare the running time of different denoising methods to evaluate their computational efficiency, as shown in Table 16. All methods take longer to process real signals because they are more complex. Among them, the EMD method takes the shortest time of 0.7630 seconds due to its simple structure, while the PSO-VMD method takes the longest time of 71.5133 seconds due to slow convergence in optimization. The proposed TOC-VMD-wavelet method takes 31.2490 seconds, achieving a better balance between denoising performance and computational efficiency than PSO-VMD.

Table 16. Running time comparison of different denoising methods for real signals.

Method	Running time (s)
PSO-VMD	71.5133
TOC-VMD-wavelet	31.2490
VMD	13.4655
EMD	0.7630

5. Conclusions

This work presents a denoising framework for neuronal spike signals that integrates TOC-optimized VMD with wavelet thresholding. The method is designed to address common challenges in electrophysiological signal recording, including noise interference, difficulty in selecting VMD parameters, and the limited adaptability of conventional denoising approaches. The performance of the proposed method is verified through experiments on both simulated and real extracellular neuronal spike signals. The results show that the TOC algorithm can quickly and steadily determine appropriate VMD parameters and reduce the limitations of traditional VMD. The kurtosis criterion helps select effective signal components and reduce signal distortion. With wavelet soft thresholding, the method achieves satisfactory denoising performance. It outperforms EMD, conventional VMD, and PSO-VMD, and achieves a better trade-off among denoising performance, waveform preservation, and computational efficiency. In addition, the method requires minimal manual parameter adjustment and is well-suited to different noise levels. It can provide reliable signals for subsequent spike detection, sorting, and neural decoding analysis.

However, the proposed method still has certain limitations. All experiments in this study are conducted on single-channel neuronal spike signals, and its performance may be affected under extremely high noise conditions. Additionally, the current validation is based only on publicly available representative datasets, and more complex physiological interference scenarios such as electrode drift and non stationary noise remain to be further tested. Future work will focus on extending the method to multi channel neural signal scenarios, enhancing its robustness under strong noise and non stationary conditions, and conducting more comprehensive cross-dataset validation and interference robustness evaluations. Furthermore, we will explore its combination with advanced deep learning-based denoising models to further improve the generalizability and practical value of the method.

Author contributions

Can Ma: Conceptualization, methodology, software, validation, writing–original draft; Zuozhi Liu: Conceptualization, supervision, writing–review and editing; Hui Li: Validation, writing–review and editing. All authors have read and agreed to the published version of the manuscript.

Use of Generative-AI tools declaration

The authors declare they have not used Artificial Intelligence tools in the creation of this article.

Acknowledgments

This work was supported by the 2025 Undergraduate and Graduate Student Scientific Research Project of Guizhou University of Finance and Economics (No. 2025BAZYSY207) and the Guizhou Postgraduate Education and Teaching Reform Project (No. 2025YJSJGXX066).

Conflict of interest

The authors have no conflict of interest that might be perceived to influence the results in this paper.

References

1. D. Reich, Spikes: Exploring the neural code, *Network-Comp. Neural*, **8** (1997), 008.
2. G. Buzsáki, C. A. Anastassiou, C. Koch, The origin of extracellular fields and currents–EEG, ECoG, LFP and spikes, *Nat. Rev. Neurosci.*, **13** (2012), 407–420.
3. M. S. Lewicki, A review of methods for spike sorting: the detection and classification of neural action potentials, *Network-Comp. Neural*, **9** (1998), R53–R78. https://doi.org/10.1088/0954-898X/9/4/001
4. K. D. Harris, D. A. Henze, J. Csicsvari, H. Hirase, G. Buzsaki, Accuracy of tetrode spike separation as determined by simultaneous intracellular and extracellular measurements, *J. Neurophysiol.*, **84** (2000), 401–414. https://doi.org/10.1152/jn.2000.84.1.401
5. R. Q. Quiroga, Z. Nadasdy, Y. Ben-Shaul, Unsupervised spike detection and sorting with wavelets and superparamagnetic clustering, *Neural Comput.*, **16** (2004), 1661–1687. https://doi.org/10.1162/089976604774201631
6. G. T. Einevoll, C. Kayser, N. K. Logothetis, S. Panzeri, Modelling and analysis of local field potentials for studying the function of cortical circuits, *Nat. Rev. Neurosci.*, **14** (2013), 770–785. https://doi.org/10.1038/nrn3599
7. X. Y. Xu, N. Chen, Y. H. Deng, T. H. Shen, N. N. Wei, S. C. Yu, et al., Enhancing neural signal quality: A spike-denoising model with BiLSTM and attention mechanism, *Brain Informatics*, **12** (2025), 28. https://doi.org/10.1186/s40708-025-00278-7
8. X. Hu, B. A. Emery, S. Khanzada, H. Amin, DENOISING: Dynamic enhancement and noise overcoming in multimodal neural observations via high-density CMOS-based biosensors, *Front. Bioeng. Biotechnol.*, **12** (2024), 1390108. https://doi.org/10.3389/fbioe.2024.1390108
9. R. X. Wang, Y. C. Xu, Y. W. Zhang, X. L. Hu, Y. Li, S. M. Zhang, A fast and effective spike sorting method based on multi-frequency composite waveform shapes, *Brain Sci.*, **13** (2023), 1156. https://doi.org/10.3390/brainsci13081156
10. P. Visu, P. S. Smitha, M. Velayutham, M. W. Ahmad, Enhanced EEG classification using adaptive DWT and heuristic-ICA algorithm, *Automatika*, **64** (2023), 827–836. https://doi.org/10.1080/00051144.2023.2208156
11. F. M. Bayer, A. J. Kozakevicius, R. J. Cintra, An iterative wavelet threshold for signal denoising, *Signal Process.*, **162** (2019), 10–20. https://doi.org/10.1016/j.sigpro.2019.04.005

12. S. Zhang, G. D. Liu, S. Q. Sun, J. Cai, Deep learning method based on multivariate variational mode decomposition for classification of epileptic signals, *Brain Sci.*, **15** (2025), 933. https://doi.org/10.3390/brainsci15090933

13. S. Raveendran, R. Kenchaiah, S. Kumar, J. Sahoo, M. K. Farsana, R. C. Mundlamuri, et al., Variational mode decomposition-based EEG analysis for the classification of disorders of consciousness, *Front. Neurosci.*, **18** (2024), 1340528. https://doi.org/10.3389/fnins.2024.1340528

14. M. Zhang, G. Wei, An integrated EMD adaptive threshold denoising method for reduction of noise in ECG, *PLoS ONE*, **15** (2020), e0235330. https://doi.org/10.1371/journal.pone.0235330

15. M. S. Fabus, A. J. Quinn, C. E. Warnaby, M. W. Woolrich, Automatic decomposition of electrophysiological data into distinct nonsinusoidal oscillatory modes, *J. Neurophysiol.*, **126** (2021), 1670–1684. https://doi.org/10.1152/jn.00344.2020

16. J. Zhou, X. M. Guo, Z. J. Wang, W. H. Du, J. Y. Wang, X. F. Han, et al., Research on fault extraction method of variational mode decomposition based on immunized fruit fly optimization algorithm, *Entropy*, **21** (2019), 400. https://doi.org/10.3390/e21040400

17. J. C. Xu, H. Y. Ma, W. He, Harmonic detection method based on parameter optimization VMD-IWT combined noise reduction, *Appl. Sci.*, **14** (2024), 5076. https://doi.org/10.3390/app14125076

18. G. Baldazzi, G. Solinas, J. D. Valle, M. Barbaro, S. Micera, L. Raffo, et al., Systematic analysis of wavelet denoising methods for neural signal processing, *J. Neural Eng.*, **17** (2020), 066016. https://doi.org/10.1088/1741-2552/abb706

19. H. G. Rey, C. Pedreira, R. Q. Quiroga, Past, present and future of spike sorting techniques, *Brain Res. Bull.*, **119** (2015), 106–117. https://doi.org/10.1016/j.brainresbull.2015.08.010

20. J. H. Wang, C. Z. Zheng, J. Qiu, X.-C. Zhong, Z. B. Bi, D. Liu, et al., An optimized VMD-wavelet denoising method for leakage detection in water supply networks from acoustic emission signals, *Int. J. Pres. Ves. Pip.*, **217** (2025), 105535. https://doi.org/10.1016/j.ijpvp.2024.105535

21. D. J. Rao, M. Huang, X. Z. Shi, Z. Yu, Z. X. He, A microseismic signal denoising algorithm combining VMD and wavelet threshold denoising optimized by BWOA, *CMES-Comp. Model. Eng.*, **141** (2024), 187–217. https://doi.org/10.32604/cmes.2024.031264

22. K. Dragomiretskiy, D. Zosso, Variational mode decomposition, *IEEE T. Signal Proces.*, **62** (2014), 531–544. https://doi.org/10.1109/TSP.2013.2288675

23. J. Kennedy, R. Eberhart, Particle swarm optimization, *Proceedings of the 1995 IEEE International Conference on Neural Networks*, Perth, WA, Australia, 1995, 1942–1948. https://doi.org/10.1109/ICNN.1995.488968

24. Y. P. Wang, S. Zhang, R. F. Cao, D. Xu, Y. Q. Fan, A rolling bearing fault diagnosis method based on the WOA-VMD and the GAT, *Entropy*, **25** (2023), 889. https://doi.org/10.3390/e25060889

25. B. Bassimir, A. Raß, R. Wanka, The convergence indicator: improved and completely characterized parameter bounds for actual convergence of particle swarm optimization, 2020, arXiv:2006.03944. https://doi.org/10.48550/arXiv.2006.03944

26. H. Faris, I. Aljarah, M. A. Al-Betar, S. Mirjalili, Grey wolf optimizer: A review of recent variants and applications, *Neural Comput. Appl.*, **30** (2018), 413–435. https://doi.org/10.1007/s00521-017-3272-5

27. K. Deb, A. Pratap, S. Agarwal, T. Meyarivan, A fast and elitist multiobjective genetic algorithm: NSGA-II, *IEEE T. Evolut. Comput.*, **6** (2002), 182–197. https://doi.org/10.1109/4235.996017

28. Y. F. Ma, Y. Ji, A combinational consensus model-based feedback mechanism for group decision-making with uncertain adjustment costs, *Group Decis. Negot.*, **35** (2026), 10.

29. Y. Ji, L. Wang, Z. S. Peng, S. J. Qu, Y. F. Han, A novel robust strategic manipulation model with tolerance and risk aversion behaviour, *J. Oper. Res. Soc.*, (2026). https://doi.org/10.1080/01605682.2026.2617488

30. M. Braik, H. Al-Hiary, H. Alzoubi, A. Hammouri, M. A. Al-Betar, M. A. Awadallah, Tornado optimizer with Coriolis force: A novel bio-inspired meta-heuristic algorithm for solving engineering problems, *Artif. Intell. Rev.*, **58** (2025), 123. https://doi.org/10.1007/s10462-025-11118-9

31. A. Rodan, A. K. Al-Tamimi, L. Al-Alnemer, S. Mirjalili, Stellar oscillation optimizer: A nature-inspired metaheuristic optimization algorithm, *Cluster Comput.*, **28** (2025), 362. https://doi.org/10.1007/s10586-024-04321-9

32. J. Antoni, The spectral kurtosis: A useful tool for characterising non-stationary signals, *Mech. Syst. Signal Pr.*, **20** (2006), 282–307. https://doi.org/10.1016/j.ymssp.2004.09.001

33. Z. Z. Liu, X. T. Wang, Q. Yuan, Robust detection of neural spikes using sparse coding based features, *Math. Biosci. Eng.*, **17** (2020), 4257–4270. https://doi.org/10.3934/mbe.2020235

34. S. Wardana, M. Melinda, R. Ramdhana, Y. Yunidar, Y. Away, N. Basir, Performance comparison of variational mode decomposition and Butterworth filtering in processing EEG signals of autism patients, *Indonesian Journal of Electronics, Electromedical Engineering, and Medical Informatics,*, **7** (2025), 461–474. https://doi.org/10.35882/ijeeemi.v7i3.105

35. W. K. Ngui, M. S. Leong, L. M. Hee, A. M. Abdelrhman, Wavelet analysis: mother wavelet selection methods, *Applied Mechanics and Materials*, **393** (2013), 953–958. https://doi.org/10.4028/www.scientific.net/AMM.393.953

36. P. Flandrin, G. Rilling, P. Goncalves, Empirical mode decomposition as a filter bank, *IEEE Signal Proc. Let.*, **11** (2004), 112–114. https://doi.org/10.1109/LSP.2003.821662

37. C. R. Liu, C. Z. Zhang, Remove artifacts from a single-channel EEG based on VMD and SOBI, *Sensors*, **22** (2022), 6698. https://doi.org/10.3390/s22176698

38. M. H. Mao, J. Chang, J. C. Sun, S. Lin, Z. H. Wang, Research on VMD-based adaptive TDLAS signal denoising method, *Photonics*, **10** (2023), 674. https://doi.org/10.3390/photonics10060674

39. B. L. Welch, The generalization of 'STUDENT'S' problem when several different population variances are involved, *Biometrika*, **34** (1947), 28–35. https://doi.org/10.1093/biomet/34.1-2.28

40. G. D. Ruxton, The unequal variance t-test is an underused alternative to Student's t-test and the Mann–Whitney U test, *Behav. Ecol.*, **17** (2006), 688–690. https://doi.org/10.1093/beheco/ark016

AIMS Press